CEAS-GNC-2022-061

CEAS EuroGNC 2022
"Conference on Guidance, Navigation and Control"
3-5 May 2022 @ Technische Universität Berlin, Germany

Hopping Maneuver between Two Satellites: Simulations, Laboratory, and Flight Experiments on the International Space Station

Daniel Watanabe Graduate student, Naval Postgraduate School, MAE Department, 93943, Monterey, CA, USA.

Stephen Kwok-Choon National Research Council Postdoctoral Research Associate, Naval Postgraduate School, MAE Department, 93943, Monterey, CA, USA. stephen.kwokchoon.mp@nps.edu

Jennifer Hudson Research Associate Professor, Naval Postgraduate School, MAE Department, 93943, Monterey, CA, USA. jennifer.hudson@nps.edu

Marcello Romano Professor , Naval Postgraduate School, MAE Department, 93943, Monterey, CA, USA.(CEAS GNC Committee Member) mromano@nps.edu

ABSTRACT

Hopping maneuvers offer a novel approach to propellantless maneuvering of small robotic spacecraft operating in the vicinity of other spacecraft. The ongoing Astrobatics project, using NASA's Astrobee free-flyer as a test platform, seeks to develop methodology by which the Astrobee robot can maneuver on-board the International Space Station using its robotic arm and gripper. This paper elaborates on the third experimental session of the Astrobatics project, which involves a self-toss maneuver in which a primary, active Astrobee performs a hopping maneuver off of a secondary, passive Astrobee. A MATLAB simulation of the maneuver was developed to analyze the hopping maneuver, and the results are compared with experimental maneuvers conducted on the Naval Postgraduate School's POSEIDYN testbed, as well as at the NASA Ames Intelligent Robotics Group granite-table laboratory. From experimental results, the magnitude and direction of the launch velocity of the primary Astrobee appear to be correlated to the release angle and are consistent with simulation results.

Keywords: Astrobee; Astrobatics; Propellantless Self-Toss Maneuvers; Lagrangian Equations of Motion; Space Robotics; TORO

Nomenclature

$AB1$, $AB2$	=	Astrobee Vehicle 1, Astrobee Vehicle 2
$\overline{CC_i}$	=	Vectors in the inertial frame between the system CoM and the CoM of the i^{th} link
$\boldsymbol{C}(\boldsymbol{x},\dot{\boldsymbol{x}})$	=	Centrifugual-Coriolis Matrix
$\overline{C_i\Gamma_i}$	=	Vectors between the link CoM and the augmented body CoM
$\overline{C_iA_{ij}}$	=	Vectors between the link CoM and the indicated joint on that link.
$\overline{F_S}$	=	Force Spring

F_D	=	Force Damping
G	=	Motor gear ratio
$\boldsymbol{H}(\boldsymbol{x})$	=	Generalized system Inertia Matrix
$i_1 ... i_4$	=	Mass moment of Inertia (kg m^2)
K_4	=	Proportional gain
$\mathbf{L}$	=	Sum of translational and rotational kinetic energies
$l_1 ... l_4$	=	Link Lengths (m)
$m_1 ... m_4$	=	Link Mass (kg)
$\underline{\underline{\mathbf{I}}}_{C_i}^{\mathscr{B}_i}$	=	i^{th} link masses and inertia tensors
ψ, θ, ϕ	=	Euler angles (heading, pitch, roll)
$\dot{\psi}, \dot{\theta}, \dot{\phi},$	=	Euler angular velocity
q_1 ... q_6	=	Generalized Coordinates (m,m,rad,rad,rad,rad)
$\dot{q}_1$ ... $\dot{q}_6$	=	Generalized Coordinate Rates (m/s,m/s,rad/s,rad/s,rad/s,rad/s)
RA	=	Release Angle
$\boldsymbol{S1 ... S5}$	=	Astrobatics Sessions 1, 2, 2a, 2b, 3a, 3b, 4, and 5 respectively
SA	=	Start Angle
τ	=	Manipulator Joint Torque Vector
T_{EP}	=	kinetic energy due to the velocity of the CoM of the entire system (N)
T_C	=	kinetic energy due to the motion of each link relative to the CoM (N)
T	=	Total kinetic energy in the system (N)
U	=	Potential Energy
$\underline{v}(C\|\mathscr{N})$	=	Velocity of the system CoM in the inertial frame
$\underline{\boldsymbol{\omega}}_{\mathscr{B}_i\mathscr{N}}$	=	angular velocity vector of the link bodies in the inertial frame.
ω_{max}	=	Maximum angular rate of the servo
$\boldsymbol{x} = [x_1, x_2, ..., x_n]^\top$	=	Generalized manipulator joint angles

1 Introduction: Robotic Hopping

As space exploration advances, more national and commercial entities seek to gain access to the opportunities and resources afforded by exploring and operating beyond Earth's atmosphere. Ref. [2–4]. With this growth, the call for more efficient means of locomotion to support these operations are necessary. Of particular interest are methods of propulsion capable of reducing the need for on-board fuel, Ref. [5–10]. Conservation of momentum requires that the amount of momentum within a system remains constant, whereby a reaction force is necessary to exert a change in velocity, ΔV, on a body.

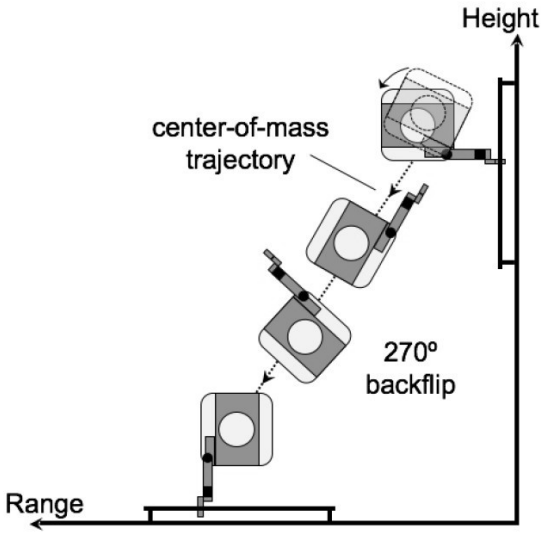

Fig. 1. Astrobatics Hop Maneuver. Ref. [1]

Hopping maneuvers, as illustrated in Fig. 1, are a method of locomotion that utilize other objects, robots, or spacecraft as the reaction mass for momentum changes. This method of locomotion could be used for longer duration missions, operation of robotic assistants aboard or around large bodies such as the ISS, including autonomous vehicles that would operate on commercial satellites. Ref. [7, 11–13]

Astrobatics is a research collaboration between the Naval Postgraduate School (NPS) Spacecraft Robotics Laboratory (SRL) and the Intelligent Robotics Group (IRG) at NASA Ames Research Center focused on the use of the Astrobee free-flying vehicle and its robotic arm to perform self-toss maneuvers. Astrobee is equipped with a 3 degree of freedom (DOF) robotic arm composed of a two-revolute-joint, two-link manipulator and a three-finger gripper end-effector (see Fig. 2). Joint 1 and Joint 2 are respectively referred to as the proximal and distal joints of the Astrobee robotic arm. A replica of the Astrobee robotic arm was used for experimental validation tests on the NPS SRL POSEIDYN (Proximity Operation of Spacecraft: Experimental hardware-In-The-loop DYNamic simulator) test-bed in preparation for test sessions performed aboard the ISS. Ref. [1, 14–19].

Outlined in Tab. 1 is a summary of the five planned Astrobatics sessions. Sessions **S1** and **S2** are completed, with **S3** (the focus of this paper) having just completed. Session **S1** involved self-toss maneuvers with a single Astrobee vehicle from a handrail on the forward wall of the ISS Japanese Experimental Module (JEM), Ref. [18]. Session **S2** compared self-toss maneuvers from a deck wall handrail, a forward wall handrail, and a free-floating initial start position, followed by an impeller stabilization to bring Astrobee to rest. Session **S3** was based on the simulation and experimental validation of a type of maneuver where an active Astrobee vehicle, AB1, was commanded to perform a self-toss from a passive free-floating Astrobee vehicle, AB2. The research challenges of the **S3** session include commanding and recording data from two Astrobee vehicles simultaneously while demonstrating a robotic self-toss from a free-floating reaction mass.

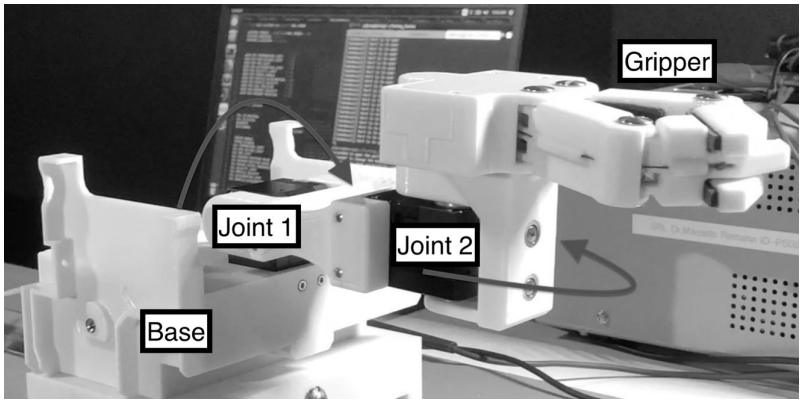

Fig. 2. NPS Replica Astrobee Arm. Joint 1 and Joint 2 are the proximal and distal joints respectively. Ref. [14]

Table 1 Summary of Astrobatics Sessions on-board the ISS

Session	Date	Vehicle	Maneuver Description
S1	Mar. 2021	AB1	Self-toss from handrail
S2a	Jul. 2021	AB1	Self-toss from handrail,
S2b	Oct. 2021	AB1	free-floating, with stabilization
S3	Nov. 2021	AB1/AB2	AB1 self-toss from AB2,
	Feb. 2022		with stabilization

This paper is focused on the **S3** session of the Astrobatics project. First, an overview of Astrobee and its capabilities shall be provided with a description of the self-toss maneuvers planned to be performed during the **S3** ISS experiments. Second, a summary of the **S3** Lagrangian Equations of Motion (EOM) modeling method is included using the MATLAB TORO software developed by Professor Marcello Romano. Third, an overview of the simulation results is provided, followed by, fourth, a comparison to experiments conducted on the NPS POSEIDYN testbed and at the NASA Ames IRG granite laboratory. The testing results include descriptions of experiment performance and limitations, and data analysis of the experimental results. Finally, fifth, a summary of the first **S3** ISS session completed, with a description of conclusions and future work.

2 Astrobee Free-flyer Vehicle and Ground Test conditions

Astrobee first launched to the ISS in April 2019, Ref.[21], its primary function is to serve as a guest science platform for research involving free-floating robotics. Astrobee is a cube-shaped vehicle that measures 317.5 mm (12.5 in) per side and weighs 6 kg (unladen), and 10 kg (minimum-mass during operation), Ref. [20, 22]. Astrobee has a range of sensors enabling it to interact with its environment and has three payload bays that allow for guest payloads. Two impellers intake air and provide propulsion through twelve nozzles. For the Astrobatics session, Astrobee was equipped with its 3 DOF perching arm module. A diagram of the Astrobee system from the *Astrobee Guest Science Guide* is shown in Fig. 3 with further information presented in Ref. [20]. In each of the **S3** ground tests, the self-toss was initialized with two free-floating vehicles gripping the same free handrail.

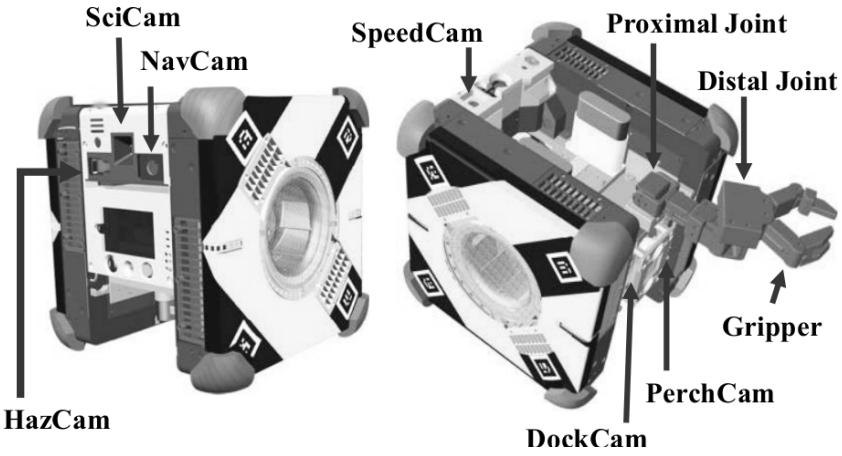

Fig. 3. NASA Astrobee Robot. Ref. [20]

The active vehicle was commanded to actuate its proximal joint from a Start Angle (SA) to a Release Angle (RA). Upon reaching the RA, the gripper end-effector was commanded to release from the handrail, causing the vehicles to move apart. The time-history of the vehicles' position and orientation after release were measured.

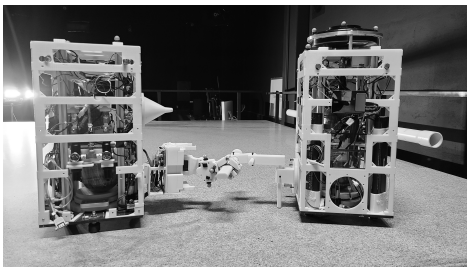

Fig. 4. Two FSS Configured for an S3 Hopping Maneuver on the POSEIDYN Testbed

2.1 NPS POSEIDYN Test Configuration

The NPS test facility used for the Astrobatics pre-flight experimentation is the POSEIDYN testbed, which consists of a 4 m x 4 m granite monolith table and Floating Spacecraft Simulator (FSS) vehicles that operate on its surface. The POSEIDYN testbed provides the ability to conduct experiments in a simulated 3 DOF low-gravity environment Ref. [23–30].

The FSS vehicles provide mounting fixtures for a variety of experimental packages, as seen on the right side of Fig. 4. The configuration for the **S3** NPS SRL self-toss experiments is shown in Fig. 4: the active vehicle is on the left with the Astrobee arm module, and the passive vehicle is on the right.

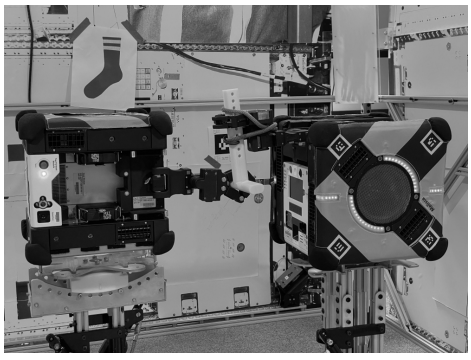

Fig. 5. NASA Ames: Astrobatics S3 configuration during IRG granite lab tests

2.2 NASA Ames IRG Test Configuration

NASA IRG have a 2 m x 2 m granite monolith table Ref. [31]. In this facility, the Astrobee free-flyer vehicles use their native sensors to perform localization and tracking. To support testing algorithms and provide an analog of the test conditions aboard the ISS, the walls of the IRG granite lab are made to resemble the interior of the JEM Kibō

module. For the **S3** IRG test session, the Active Astrobee, AB1, was on placed on its side so that it proximal joint could move parallel to the granite surface. To make use of available mounting hardware, the Passive Astrobee, AB2, was placed in the upright orientation. A custom T-bar handrail was used as the grasping interface between both Astrobee vehicles, as shown in Fig. 5.

3 Lagrangian Equations of Motion

We assume the space system has zero initial linear and angular momenta; orbital effects are neglected for the short duration of the robotic maneuver. As there are no external forces acting on the system, its center of mass does not accelerate and the linear and angular momenta of the system are conserved.

The equations of motion for a free-floating space robot can be applied to the space system. Following the approach of Ref. [32], the equations of motion are

$$\boldsymbol{H}(\boldsymbol{x})\ddot{\boldsymbol{x}} + \boldsymbol{C}(\boldsymbol{x},\dot{\boldsymbol{x}})\dot{\boldsymbol{x}} = \boldsymbol{\tau} \tag{1}$$

where $\boldsymbol{H}(\boldsymbol{x})$ is the generalized system inertia matrix, $\boldsymbol{C}(\boldsymbol{x},\dot{\boldsymbol{x}})$ is the Centrifugal-Coriolis matrix, and $\boldsymbol{\tau}$ is the manipulator joint torque vector. The manipulator joint angles form the vector $\boldsymbol{x} = [x_1, x_2, ..., x_n]^T$.

The generalized inertia matrix can be found using a Lagrangian approach,

$$\boldsymbol{H}(\boldsymbol{x}) = \frac{d}{dt}\left(\frac{d\boldsymbol{L}}{d\dot{\boldsymbol{x}}}\right) - \frac{d\boldsymbol{L}}{d\boldsymbol{x}} \tag{2}$$

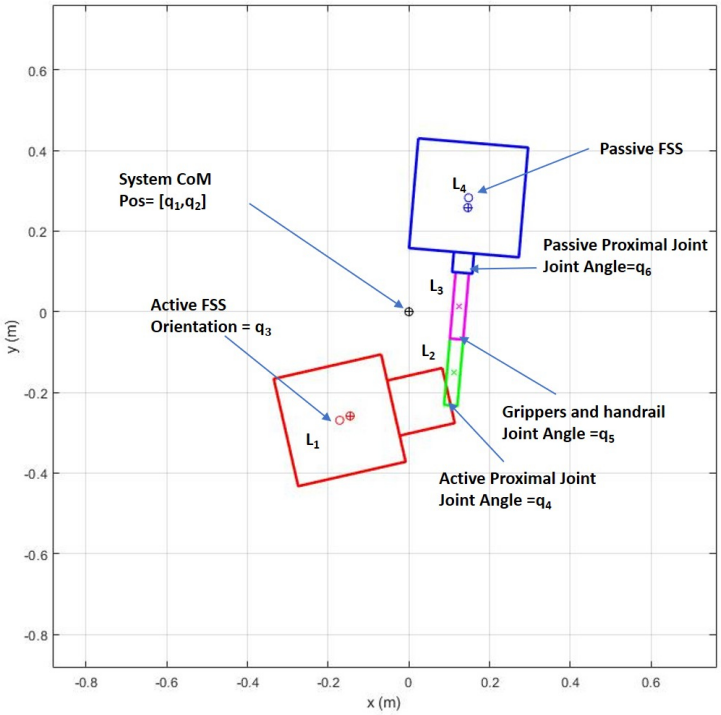

Fig. 6. FSS Toss Phase Diagram: The system Center of Mass (CoM) is defined by q_1 and q_2. Joint angles are given as angular displacement relative to the previous link with the exception of q_3, which is given relative to the inertial frame.

Here, $\boldsymbol{L}$ is the sum of the translational and rotational kinetic energies of all moving bodies in the space system; the potential energy of the system is zero.

3.1 Modeling Method

The **S3** self-toss maneuver was split into a *toss* and *coast* phase. The *toss* phase began while both Astrobee vehicles gripped the handrail and was modeled as a single 4-link, 6 DOF system, whereby the dynamics of the system were propagated under the effect of AB1's joint actuation. The *toss* phase was completed when the gripper actuated and the passive Astrobee, AB2, was released from the active Astrobee, AB1. The *coast* was defined as the period after release. During the *coast*, the Astrobees were modeled as two separate, 2-link, 4 DOF systems. The two 4 DOF systems were considered free floating and maintained the rotational and linear inertia imparted during the *toss* phase with no additional internal or external forces. The gripper was assumed to instantly release and not induce any further contact forces on the system. The simulation of the *toss* and *coast* phase was implemented using the MATLAB Toolset for Orbital RObotics (TORO) software, Ref.[33]. The virtual manipulator method, while not strictly necessary to simulate the 4-link system during the *toss*, made it possible to calculate each individual link's momentum for the *coast*.

Table 2 Symbolic Variables

Variable Symbol	Variable Definition	Unit
l_1 ... l_4	Link lengths	m
m_1 ... m_4	Link Mass	kg
ic_1 ... ic_4	Mass moment of inertia	kg m^2
q_1 ... q_6	Generalized Coordinates	Various
$\dot{q}_1$ ... $\dot{q}_6$	Generalized Coordinate Rates	Various

3.2 The *Toss* Phase

The kinetic and potential energy of the system was defined as a function of the generalized coordinates q_n, link dimensions (l_i), masses (m_i), and inertias (I_i). Shown in Fig. 6 the red and blue squares indicate AB1 and AB2 respectively, while the green and magenta rectangles represent the Astrobee manipulators past the proximal joint. The system was oriented in the plane of motion of the Astrobee proximal joints; the distal joints were considered fixed.

The Center of Mass (CoM), C, was defined by q_1 and q_2 and shown as a black circle with a cross. q_3 was defined as the angle of rotation of the active FSS, AB1, with respect to the inertial frame, and the coordinates q_4, q_5, and q_6 are the joint angles between the active FSS and the first arm, the first and the second arm, and the second arm and the passive FSS, respectively.

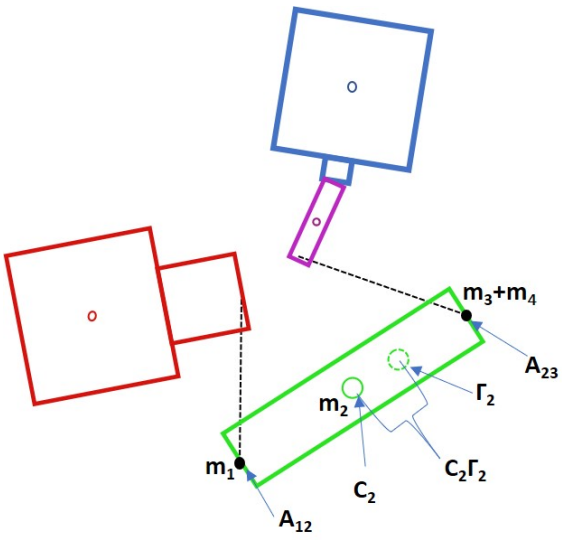

Fig. 7. Augmented Body Illustration: Shown explicitly for link 2, the augmented body places the masses of previous and following links at the joint positions. This shifts the link's CoM to the augmented body CoM denoted by a Γ.

The velocity of the system CoM in the inertial frame is $\underline{v}(C|\mathcal{N})$, and the vectors in the inertial frame between the system CoM and the CoM of the i^{th} link were defined by $\underline{CC_i}$. The kinetic energy of the system in terms of the generalized coordinates and parameters is given by Eq. (3 - 5) are defined in *Orbital Space Robotics* Ref. [33]. The total kinetic energy is

$$T = T_{EP} + T_C \tag{3}$$

where T_{EP} is defined as the kinetic energy due to the velocity of the CoM of the entire system while the term T_C is the kinetic energy due to the motion of each link relative to the CoM. Here, in addition to previously defined terms, m_i and $\underline{\underline{\mathbf{I}}}_{C_i}^{\mathcal{B}_i}$ are the i^{th} link masses and inertia tensors, and the term $\underline{\omega}_{\mathcal{B}_i\mathcal{N}}$ is the angular velocity vector of the link bodies in the inertial frame.

$$T_{EP} = \frac{1}{2} M \underline{v}(C|\mathcal{N}) \cdot \underline{v}(C|\mathcal{N}) \tag{4}$$

$$T_C = \frac{1}{2}\sum_{i=1}^{n} m_i \frac{d}{dt}\bigg|_{\mathcal{N}} \underline{CC_i} \cdot \frac{d}{dt}\bigg|_{\mathcal{N}} \underline{CC_i} + \frac{1}{2}\sum_{i=1}^{n} \underline{\omega}_{\mathcal{B}_i\mathcal{N}} \cdot \underline{\underline{\mathbf{I}}}_{C_i}^{\mathcal{B}_i} \cdot \underline{\omega}_{\mathcal{B}_i\mathcal{N}} \tag{5}$$

To use the virtual manipulator method, the use of augmented bodies needs to be implemented. In this application, an augmented body refers to each of the links in the system with the link's CoM calculated as if the mass of the previous and proceeding attached links are point masses collocated at the link joints.

Using Equation (6) for a four-body system [33], the vectors between the standard link CoM and the augmented body CoM were calculated for each of the bodies. m_i indicates the mass of each individual link and M indicates the total system mass. The vectors $\underline{C_i\Gamma_i}$ indicate the vectors between the link CoM and the augmented body CoM, while the vectors indicated by $\underline{C_iA_{ij}}$ are the vectors between the link CoM and the indicated joint on that link. An illustration of the second link's augmented body is shown in Fig. 7.

$$\begin{aligned}
\underline{C_1\Gamma_1} &= \left(\frac{m_2+m_3+m_4}{M}\right)\underline{C_1A_{12}} & \underline{C_3\Gamma_3} &= \left(\frac{m_1+m_2}{M}\right)\underline{C_3A_{23}} + \left(\frac{m_4}{M}\right)\underline{C_3A_{34}} \\
\underline{C_2\Gamma_2} &= \left(\frac{m_1}{M}\right)\underline{C_2A_{12}} + \left(\frac{m_3+m_4}{M}\right)\underline{C_2A_{23}} & \underline{C_4\Gamma_4} &= \left(\frac{m_1+m_2+m_3}{M}\right)\underline{C_4A_{34}}
\end{aligned} \tag{6}$$

Using the Wittenburg formula from Ref. [33] in Equation (7), the vectors indicating the displacement between the common system CoM and each individual link CoM were calculated.

$$\begin{aligned}
\underline{CC_1} &= \underline{\Gamma_1C_1} + \underline{\Gamma_2A_{12}} + \underline{\Gamma_3A_{23}} + \underline{\Gamma_4A_{34}} & \underline{CC_3} &= \underline{\Gamma_1A_{12}} + \underline{\Gamma_2A_{23}} + \underline{\Gamma_3C_3} + \underline{\Gamma_4A_{34}} \\
\underline{CC_2} &= \underline{\Gamma_1A_{12}} + \underline{\Gamma_2C_2} + \underline{\Gamma_3A_{23}} + \underline{\Gamma_4A_{34}} & \underline{CC_4} &= \underline{\Gamma_1A_{12}} + \underline{\Gamma_2A_{23}} + \underline{\Gamma_3A_{34}} + \underline{\Gamma_4C_4}
\end{aligned} \tag{7}$$

The time derivatives of these displacement vectors were then used to determine the kinetic energy of the system, where the angular velocities of each link relative to the inertial frame are indicated by $\underline{\omega_{Li\mathcal{N}}}$ and iterated within TORO, Ref. [33].

$$\begin{aligned}
\underline{C\dot{C}_1} &= \underline{\omega_{L1\mathcal{N}}} \times \underline{\Gamma_1C_1} + \underline{\omega_{L2\mathcal{N}}} \times \underline{\Gamma_2A_{12}} + \underline{\omega_{L3\mathcal{N}}} \times \underline{\Gamma_3A_{23}} + \underline{\omega_{L4\mathcal{N}}} \times \underline{\Gamma_4A_{34}} \\
\underline{C\dot{C}_2} &= \underline{\omega_{L1\mathcal{N}}} \times \underline{\Gamma_1A_{12}} + \underline{\omega_{L2\mathcal{N}}} \times \underline{\Gamma_2C_2} + \underline{\omega_{L3\mathcal{N}}} \times \underline{\Gamma_3A_{23}} + \underline{\omega_{L4\mathcal{N}}} \times \underline{\Gamma_4A_{34}} \\
\underline{C\dot{C}_3} &= \underline{\omega_{L1\mathcal{N}}} \times \underline{\Gamma_1A_{12}} + \underline{\omega_{L2\mathcal{N}}} \times \underline{\Gamma_2A_{23}} + \underline{\omega_{L3\mathcal{N}}} \times \underline{\Gamma_3C_3} + \underline{\omega_{L4\mathcal{N}}} \times \underline{\Gamma_4A_{34}} \\
\underline{C\dot{C}_4} &= \underline{\omega_{L1\mathcal{N}}} \times \underline{\Gamma_1A_{12}} + \underline{\omega_{L2\mathcal{N}}} \times \underline{\Gamma_2A_{23}} + \underline{\omega_{L3\mathcal{N}}} \times \underline{\Gamma_3A_{34}} + \underline{\omega_{L4\mathcal{N}}} \times \underline{\Gamma_4C_4}
\end{aligned} \tag{8}$$

$$\text{where: } \underline{\omega_{Ln\mathcal{N}}} = \sum_{i=3}^{n+2} \dot{q}_i \text{ , } \dot{\theta}_i = \text{norm}(\underline{\omega_{Li\mathcal{N}}}) \text{ , and : } \mathbf{n}_\times = \begin{bmatrix} 0 & -1 \\ 1 & 0 \end{bmatrix} \tag{9}$$

An additional conversion was made to convert all the vectors into the same frame. The frame of the first link $\{\hat{e}^{L1}\}$ will be used for convenience Ref. [33]. A Direction Cosine Matrix (DCM) was used to convert between the various link frames, where $\mathbf{C}_{Li}^{Lj}$ was the DCM from the link i frame to the link j frame. For conciseness, the angular velocities were reduced to the scalar value of the z-component, $\dot{\theta}_i$, of the total angular velocity. Since the simulation was designed to remain in the xy-plane, the value of the z-component was determined as shown in Equation (9). The adapted equation for the time derivatives in the AB1, L1 frame is shown in Equation (10), Ref. [33].

$$\begin{aligned}
[\underline{C\dot{C}_1}]^{L1} &= \dot{\theta}_1\mathbf{n}_\times[\underline{\Gamma_1C_1}]^{L1} + \dot{\theta}_2\mathbf{n}_\times\mathbf{C}_{L2}^{L1}[\underline{\Gamma_2A_{12}}]^{L2} + \dot{\theta}_3\mathbf{n}_\times\mathbf{C}_{L3}^{L1}[\underline{\Gamma_3A_{23}}]^{L3} + \dot{\theta}_4\mathbf{n}_\times\mathbf{C}_{L4}^{L1}[\underline{\Gamma_4A_{34}}]^{L1} \\
[\underline{C\dot{C}_2}]^{L1} &= \dot{\theta}_1\mathbf{n}_\times[\underline{\Gamma_1A_{12}}]^{L1} + \dot{\theta}_2\mathbf{n}_\times\mathbf{C}_{L2}^{L1}[\underline{\Gamma_2C_2}]^{L2} + \dot{\theta}_3\mathbf{n}_\times\mathbf{C}_{L3}^{L1}[\underline{\Gamma_3A_{23}}]^{L3} + \dot{\theta}_4\mathbf{n}_\times\mathbf{C}_{L4}^{L1}[\underline{\Gamma_4A_{34}}]^{L1} \\
[\underline{C\dot{C}_3}]^{L1} &= \dot{\theta}_1\mathbf{n}_\times[\underline{\Gamma_1A_{12}}]^{L1} + \dot{\theta}_2\mathbf{n}_\times\mathbf{C}_{L2}^{L1}[\underline{\Gamma_2A_{23}}]^{L2} + \dot{\theta}_3\mathbf{n}_\times\mathbf{C}_{L3}^{L1}[\underline{\Gamma_3C_3}]^{L3} + \dot{\theta}_4\mathbf{n}_\times\mathbf{C}_{L4}^{L1}[\underline{\Gamma_4A_{34}}]^{L1} \\
[\underline{C\dot{C}_4}]^{L1} &= \dot{\theta}_1\mathbf{n}_\times[\underline{\Gamma_1A_{12}}]^{L1} + \dot{\theta}_2\mathbf{n}_\times\mathbf{C}_{L2}^{L1}[\underline{\Gamma_2A_{23}}]^{L2} + \dot{\theta}_3\mathbf{n}_\times\mathbf{C}_{L3}^{L1}[\underline{\Gamma_3A_{34}}]^{L3} + \dot{\theta}_4\mathbf{n}_\times\mathbf{C}_{L4}^{L1}[\underline{\Gamma_4C_4}]^{L1}
\end{aligned} \tag{10}$$

The total kinetic energy of the system was then formulated in Equation (11).

$$T_{EP} = \frac{1}{2}M(\dot{q}_1^2 + \dot{q}_2^2) \qquad T_C = \frac{1}{2}\sum_{i=1}^{4} m_i([\underline{C\dot{C}_i}]^{L1})'[\underline{C\dot{C}_i}]^{L1} + \frac{1}{2}\sum_{i=1}^{4} I_i\dot{\theta}_i{}^2 \qquad T = T_{EP} + T_C \tag{11}$$

The system was constrained to a horizontal plane (both in the simulation and in experimentation on the granite table lab), the total potential energy, U, of the system was set as $U = 0$. This simulation was meant to reflect the NPS FSS, however, a small offset needs to be added to reflect the mounting hardware between the main body and the arms shown in Equation 12.

$$\begin{aligned} \underline{C_1A_{12}} &= \left[\tfrac{l1}{2} + 0.14, -0.025\right]^\top & \underline{C_2A_{23}} &= -\underline{C_2A_{12}} & \underline{C_3A_{34}} &= -\underline{C_3A_{23}} \\ \underline{C_2A_{12}} &= \left[-\tfrac{l2}{2}, 0\right]^\top & \underline{C_3A_{23}} &= \left[-\tfrac{l3}{2}, 0\right]^\top & \underline{C_4A_{34}} &= \left[-\tfrac{l4}{2} - 0.05, 0\right]^\top \end{aligned} \tag{12}$$

3.3 The *Coast* Phase

Developing the EOM for the *coast* phase follows a nearly identical process as the toss phase. The difference is the decrease in complexity from a 6 DOF system to two separate 4 DOF systems. Each of the two FSS two-body simulations was formulated and run separately using initial conditions provided by the toss phase simulation. Starting with formulation of the augmented body vectors in Equation 13, the formulation is immediately simpler than those in Equation 6 developed for the toss phase. This simplicity carries through to Equation 14.

$$\underline{C_1\Gamma_1} = \left(\frac{m_2}{M}\right)\underline{C_1A_{12}} \qquad \underline{C_2\Gamma_2} = \left(\frac{m_1}{M}\right)\underline{C_2A_{12}} \tag{13}$$

$$\mathbf{C}_{L2}^{L1} = \begin{bmatrix} cos(q_4) & -sin(q_4) \\ sin(q_4) & cos(q_4) \end{bmatrix} \qquad \begin{aligned} [\underline{C\dot{C}_1}]^{L1} &= \dot{\theta}_1 \mathbf{n}_\times [\underline{\Gamma_1 C_1}]^{L1} + \dot{\theta}_2 \mathbf{n}_\times \mathbf{C}_{L2}^{L1} [\underline{\Gamma_2 A_{12}}]^{L2} \\ [\underline{C\dot{C}_2}]^{L1} &= \dot{\theta}_1 \mathbf{n}_\times [\underline{\Gamma_1 A_{12}}]^{L1} + \dot{\theta}_2 \mathbf{n}_\times \mathbf{C}_{L2}^{L1} [\underline{\Gamma_2 C_2}]^{L2} \end{aligned} \tag{14}$$

The energy equations remain nearly identical to the equations used in the toss phase, but there are fewer terms in the kinetic energy equation.

$$T_{EP} = \frac{1}{2}M(\dot{q}_1^2 + \dot{q}_2^2) \qquad T_C = \frac{1}{2}\sum_{i=1}^{2} m_i([\underline{C\dot{C}_i}]^{L1})'[\underline{C\dot{C}_i}]^{L1} + \frac{1}{2}\sum_{i=1}^{2} I_i \dot{\theta}_i^{\,2} \qquad T = T_{EP} + T_C \tag{15}$$

3.4 Force Modeling

For the proximal joint, both the Astrobee robotic arm and the NPS FSS use Dynamixel MX-106 servos. The manufacturer specifies a gear ratio of 212.6:1 [34]. Experimental data for the servo's static friction coefficient and damping ratio (0.1170 and 0.0414 respectively) are provided in Ref. [35]. The static friction and damping torque were initially set by Equations (16 - 17), where G is the gear ratio and $\dot{q}$ is the angular rate of the joint, then further adjusted as needed.

$$F_S = 0.1179G = 25.07\ Nm \tag{16}$$

$$F_D = 0.0414\dot{q} = 8.8\dot{q}\ Nm \tag{17}$$

The force applied to joint 1 (the proximal joint on the active FSS) was modelled using the advertised maximum angular rate of the servo, ω_{max}, and a pseudo-proportional controller was developed to create a force value at each time step. The equation used for this controller is shown in Equation (18).

$$f_4 = K_4(\omega_{max} - \dot{q}_4) \tag{18}$$

The value for the proportional gain, K_4, can be set at any reasonable value that works with the simulation; however, it can be fine-tuned using experimental data to match the settling time.

4 Results

4.1 TORO S3 Simulation Results

For the NPS FSS **S3** simulation, the initial parameters are listed in Table 3. The generalized and initial coordinate velocities were set to zero with the exception of q_4, which corresponds to the proximal joint position of the active FSS. The value of q_4 was defined to match the starting joint angle for the desired toss maneuver. An example toss maneuver with an initial joint angle of 90° is shown in Tab. 3.

Table 3 Initial Parameter Variables for Toss phase

Var.	l_1	l_2	l_3	l_4	m_1	m_2	m_3	m_4	ic_1	ic_2	ic_3	ic_4
Value	0.273	0.165	0.165	0.273	10	1	1	10	0.124	0.002	0.002	0.124
Units	m	m	m	m	kg	kg	kg	kg	kg m^2	kg m^2	kg m^2	kg m^2
Var.	q_1	q_2	q_3	q_4	q_5	q_6	$\dot{q}_1$	$\dot{q}_2$	$\dot{q}_3$	$\dot{q}_4$	$\dot{q}_5$	$\dot{q}_6$
Value	0	0	0	$\frac{\pi}{2}$	0	0	0	0	0	0	0	0
Units	m	m	rad	rad	rad	rad	$\frac{m}{s}$	$\frac{m}{s}$	$\frac{rad}{s}$	$\frac{rad}{s}$	$\frac{rad}{s}$	$\frac{rad}{s}$

Table 4 Initial Parameter Variables for *Coast* Phase from Toss Phase

	Active Astrobee: AB1				Passive Astrobee: AB2			
Var.	$q_{1_{FSS1}}$	$q_{2_{FSS1}}$	$q_{3_{FSS1}}$	$q_{4_{FSS1}}$	$q_{1_{FSS2}}$	$q_{2_{FSS2}}$	$q_{3_{FSS2}}$	$q_{4_{FSS2}}$
Value	$\underline{R}_{FSS1}(1)$	$\underline{R}_{FSS1}(2)$	q_3	q_3+q_4	$\underline{R}_{FSS2}(1)$	$\underline{R}_{FSS2}(2)$	$q_3+q_4+q_5+q_6$	q_6
Var.	$\dot{q}_{1_{FSS1}}$	$\dot{q}_{2_{FSS1}}$	$\dot{q}_{3_{FSS1}}$	$\dot{q}_{4_{FSS1}}$	$\dot{q}_{1_{FSS2}}$	$\dot{q}_{2_{FSS2}}$	$\dot{q}_{3_{FSS2}}$	$\dot{q}_{4_{FSS2}}$
Value	$\dot{\underline{R}}_{FSS1}(1)$	$\dot{\underline{R}}_{FSS1}(2)$	$\dot{q}_3$	$\dot{q}_3+\dot{q}_4$	$\dot{\underline{R}}_{FSS2}(1)$	$\dot{\underline{R}}_{FSS2}(2)$	$\dot{q}_3+\dot{q}_4+\dot{q}_5+\dot{q}_6$	$\dot{q}_6$

An end time, t_f, was passed to the *toss* phase simulation script, which returned a time array from $t = 0$ to $t = t_f$, whose results were then used to initiate the *coast* phase. Using Equations 6 - 7 and the body vectors defined in Equation 12, the positions of each link CoM are determined relative to the system CoM.

$$\underline{C_i} = \underline{CC_i} + \begin{bmatrix} q_1 & q_2 \end{bmatrix}^\top \qquad \underline{R}_{FSS1} = \frac{m_1\underline{C_1} + m_2\underline{C_2}}{m1+m2} \qquad \underline{R}_{FSS2} = \frac{m_3\underline{C_3} + m_4\underline{C_4}}{m3+m4} \tag{19}$$

$$q_{3_{FSS1}} = q_3 \qquad q_{4_{FSS1}} = q_3+q_4 \qquad q_{3_{FSS2}} = q_3+q_4+q_5+q_6 \qquad q_{4_{FSS2}} = q_6 \tag{20}$$

These position vectors relative to the system CoM can then be converted to the inertial frame by adding them to the position of the system CoM, which is defined by q_1 and q_2. This conversion was shown in Equation 19 where $\underline{C_i}$ is the position of link i relative to the origin.

The position of each link was converted into the positions of the CoM of each, now separate, FSS using Equation 19, where $\underline{R}_{FSSi}$ was defined as the position vector of the i^{th} FSS CoM from the origin. $\underline{R}_{FSSi}$ provides the first two generalized coordinates for each of the FSS. To generate the remaining generalized coordinates, the coordinates of the final state of the toss phase can be summed down the line by adding the joint angles for each link with the exception of FSS1's q_5, which is the q_6 from the toss phase. Coordinate rates are generated in a similar manner by adding the joint angle rates from the end of the toss phase. The velocity of the FSS CoM was generated by taking the differences of the final two time steps and dividing them by the step size. The initial conditions provided to the two single FSS *coast* phase simulations are outlined in Tab. 4.

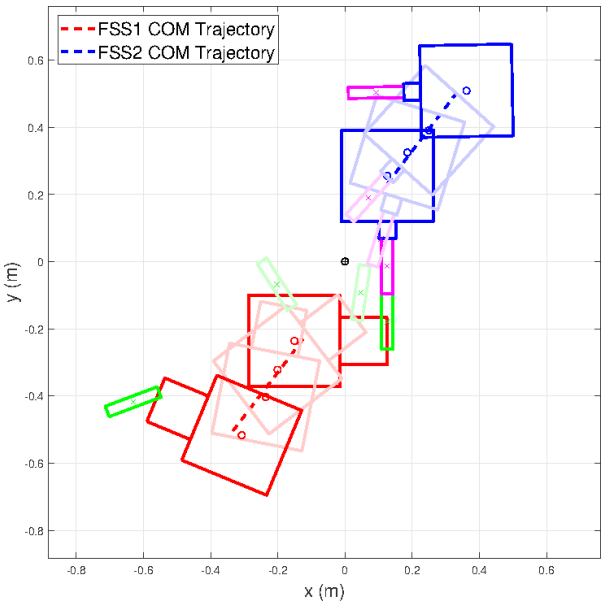

(a) SIM: Simulation Active FSS (Red) & Passive FSS (Blue). Active FSS Proximal Joint Commanded 90 to 45 Degrees

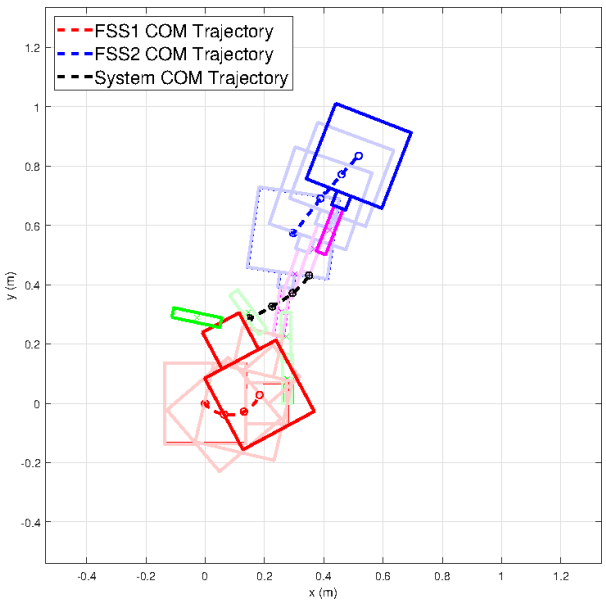

(b) EXP: NPS Experimental Self-Toss Of active FSS (red) from passive FSS (blue). Active FSS Proximal Joint commanded from SA $= 90°$ **RA** $= 45°$

Fig. 8. Comparison Simulation to Experimental

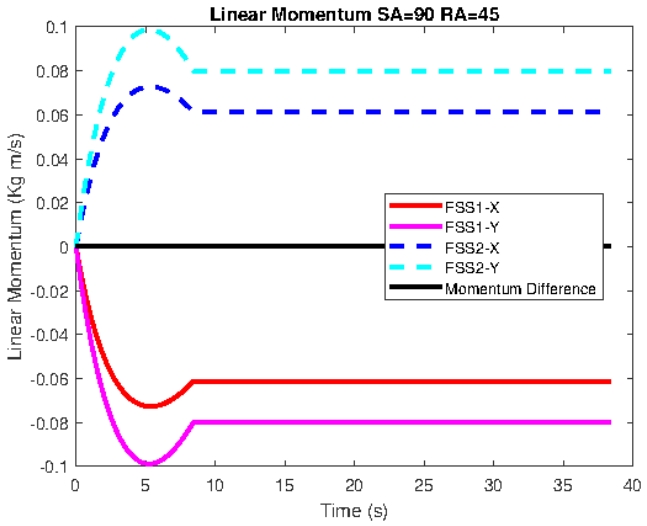

(a) SIM: Simulation Linear Momentum

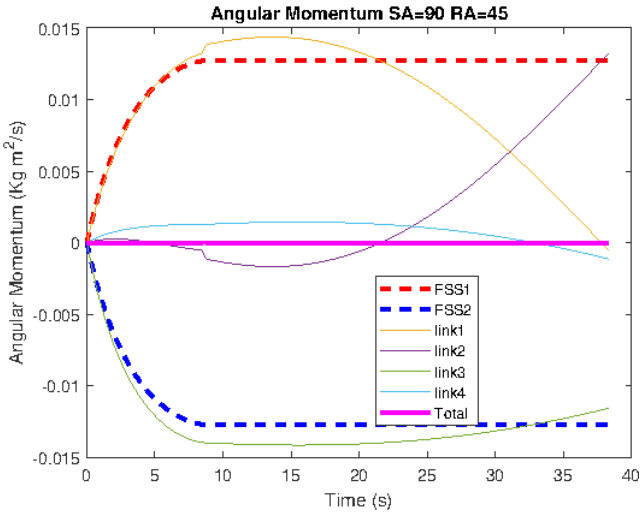

(b) SIM: Simulation Angular Momentum

Fig. 9. SIM: Linear and Angular Momentum

Using the positions and orientations over time of each link allows the entire toss maneuver to be plotted for visual reference as seen in Fig. 8a. The red squares indicate AB1 and its mounting bracket, the blue squares indicate AB2 and its mounting bracket, and the green and magenta rectangles are the corresponding arms past the proximal joint. The plot shows the initial and final positions of both FSS units as well as "ghost" positions at 10-second intervals. The dashed red and blue lines indicate the trajectories of the FSS. The stationary black circle and cross indicates that momentum was conserved during the maneuver.

This provides an immediate visual check that conservation of momentum is conserved. Fig. 9a shows a comparison of the linear momentum of each FSS in both the X and the Y directions. Here, the conservation of momentum is directly observed.

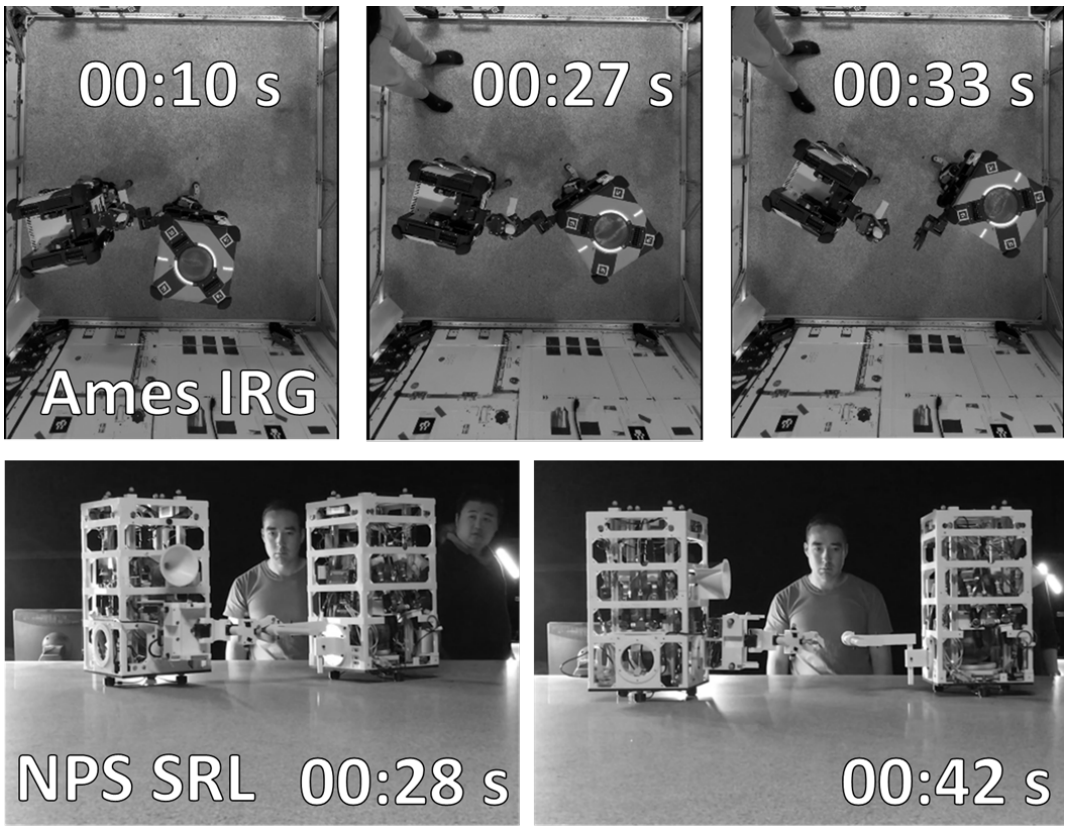

Fig. 10. SRL NPS and NASA Ames S3 Experiment

As discussed in previous section in regards to splicing the data of the *coast* and *toss* phase, the data in Fig. 9a and all future data plots include the results of both phases combined into a single continuous data array. Directly plotting the absolute value of the linear momentum and angular momenta of each individual link in Fig. 9a and 9b can further prove that momentum is conserved. The system CoM remains constant throughout the entire simulation. The CoM of each FSS move in opposite directions. Thus the data appears to show that the simulation is a physically accurate representation of a two-body self-toss maneuver.

4.2 NPS SRL Experimental Session

Several validation experimental runs were performed on the POSEIDYN testbed using two FSS vehicles in the configuration shown in Fig. 4, Fig. 10. Three sets of proximal toss experiments were conducted, each from a Start Angle, SA, of 90 ° to a Release Angle, RA, of $[60, 45, 30]^\circ$ respectively. One example of the measured results is shown in Fig. 8b.

The experiments show similar self-toss trajectories as compared to the simulation; however, there appears to be a drift of the system CoM as denoted by the dashed black line in Fig. 8b. During the series of experiments, it was observed that the arm appeared to slow as it approached the RA prior to gripper release. This may have affected

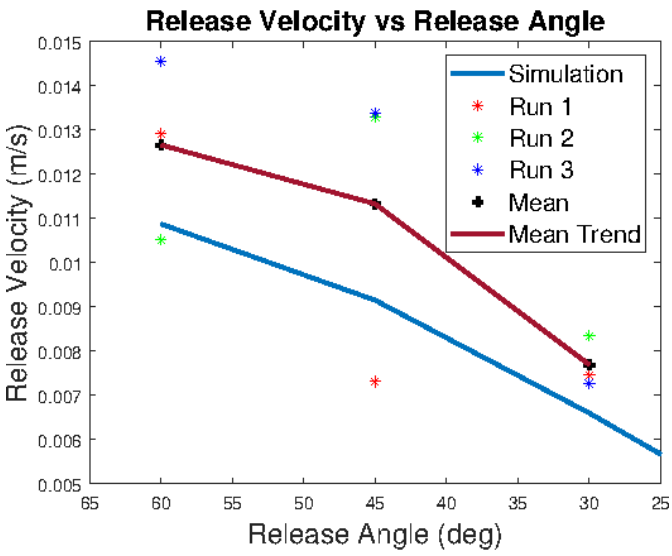

Fig. 11. EXP: Comparison of NPS Experimental Results to Simulation, where Active FSS proximal joint commanded from SA $= 90^\circ$ to RA $= 45^\circ$: Run 1

the launch trajectory of both the active and passive FSS vehicles, causing differences between the simulations and test results.

A comparison plot of the release linear velocity vs release angle for the experimental runs compared to simulation is shown in Fig. 11. The linear velocity at release for the nine experimental runs, separated by release angle, is plotted and compared to the mean simulation result found from simulation.

4.3 NASA Ames IRG Session

In preparation for the **S3** session aboard the ISS, a series of self-toss maneuvers were performed at the IRG granite lab. An example run where the start angle, SA, was -20° to the release angle, RA, of 0° is shown in Fig. 12 and Fig. 10. During the test session, it was observed that there was a movement bias on the granite table, where the trajectories of both vehicles during each run moved to the top right corner of the granite table.

Possible reasons for the bias could be damaged air-bearing pads, a misalignment of the granite table, or perhaps an air pressure differential in the room. To counteract the movement bias, the relative motion of each vehicle was the plotted with respect to the system CoM as shown in Fig. 12. In so doing, the results from the POSEIDYN FSS experiments compare quite favorably to those recorded on the Ames IRG granite table. The data recorded from the Astrobees' onboard sensors is obtained by visual recognition of features in its surroundings, which differs from the external Vicon cameras used in the NPS SRL. The release velocities (both angular and linear) for each time step were calculated by dividing the displacement between the experiment start and current time elapsed. This provided an average release velocity that was then used to plot and compare the simulation vs. experimental direction vectors as shown in Fig. 13.

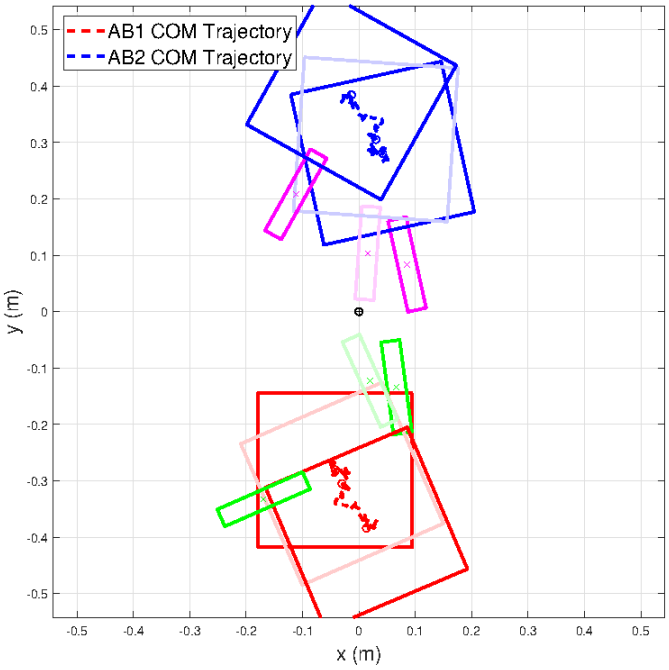

Fig. 12. EXP: Experiment at NASA Ames IRG, active (red) astrobee proximal joint command SA $= -20^\circ$ to RA $= 0^\circ$

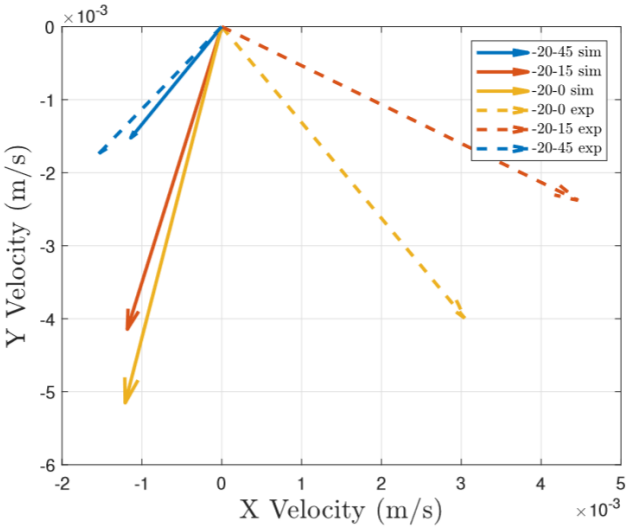

Fig. 13. Comparison of Linear Velocity vector Directions: Simulation Vs. NASA Ames IRG Experiment

As shown in Fig. 13, the launch directions of the experiment results were offset from the simulation results in roughly the same direction as the offset observed during the POSEIDYN tests. The offset in the launch trajectory as compared to simulation may have been caused by similar joint actuation behaviour as observed in the NPS SRL **S3** session, here the proximal joint slowed down as it approached the desired release angle. This, coupled with possible gripper contact interaction during release, could explain the discrepancy in the simulation to experimental velocity vector for each self-toss maneuver.

4.4 ISS Test

Fig. 14 is a visualization of the **S3** self-toss maneuver of the active astrobee (red) from the passive astrobee (blue). Upon self-toss, similar to the **S3** runs performed at NPS Spacecraft Robotics Laboratory and the NASA Ames Intelligent Robotics Group Astrobee testbed. The active Astrobee launches itself away from the passive Astrobee, during release both Astrobees rotate off the expected axis of actuation this could be due to the contact dynamic effects between the gripper end-effector and handrail.

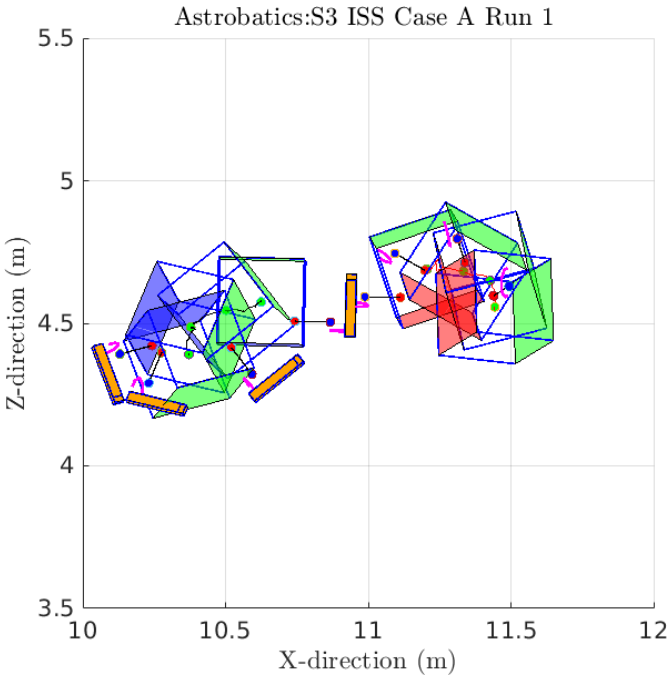

Fig. 14. Time Lapse of S3 self-toss onboard the ISS

Shown in Fig. 15a and Fig. 15b is the position and velocity of the active (red) and passive (blue) Astrobee vehicles during the **S3** self-toss maneuver. The self-toss and release occurs after the first 15 seconds from the start of the maneuver.

The photo in Fig. 16 was taken during the **S3** session aboard the ISS on November 23, 2021. As shown, the active Astrobee, Bumble (AB1), is on the left with the NPS skin, and the passive Astrobee, Queen (AB2), is on the right with the green skin. For each experimental run, the Astrobee vehicles were brought to rest and made to grab onto a common free-floating handrail at their initial start angles. At the start of the **S3** maneuver, the free-floating system

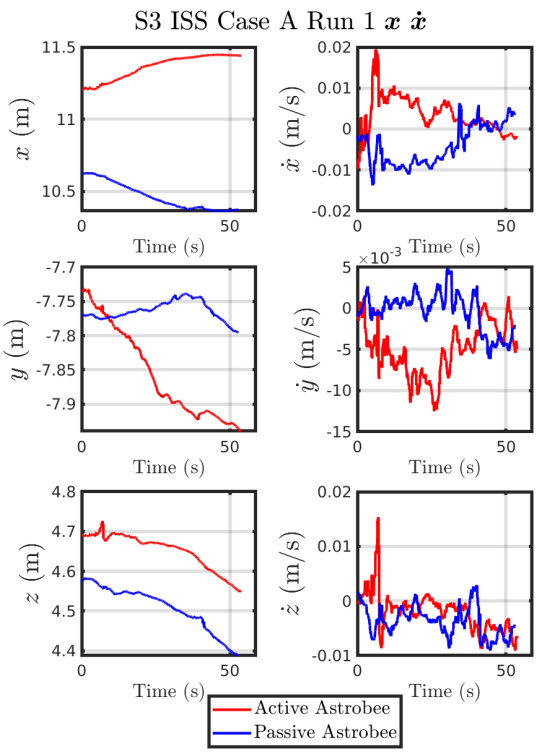

(a) Plots of position and velocity of the active and passive astrobee vehicle during self-toss maneuver

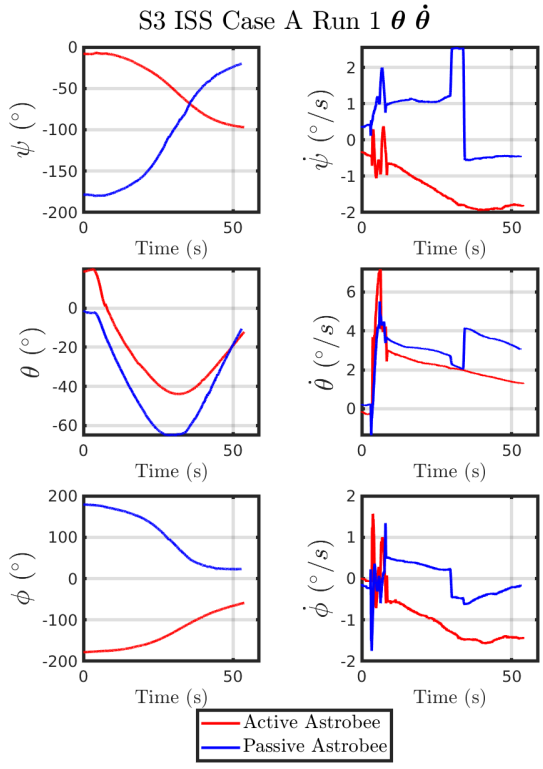

(b) Plots of angular position and rate of the active and passive astrobee vehicle during self-toss maneuver

Fig. 15. S3 self-toss maneuver onboard the ISS

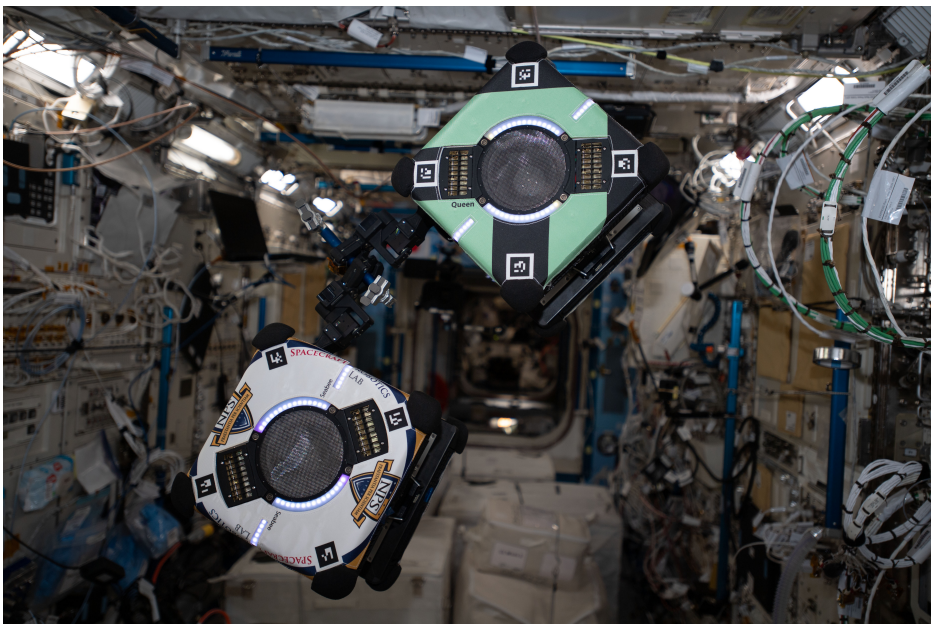

Fig. 16. Photo of S3 configuration during ISS session. (Credit NASA Ref. [36])

was released, and both AB1 and AB2 were commanded to start localization data capture, followed by AB1 performing the self-toss whilst AB2 was passively recording.

5 Conclusion

This paper presents a Conservation of Momentum Lagrangian method to simulate a self-toss maneuver of an active free-floating vehicle performing a self-toss maneuver from a passive free-floating object. Experimental validation was performed in the NPS SRL laboratory and at the NASA Ames IRG granite lab test facility to compare the theoretical model to the granite lab tests. This was done in preparation for an experimental session on-board the International Space Station. Overall, the simulation and granite lab tests show a correlation. However, the TORO simulation assumed perfect release of the passive object from the active vehicle with no further disturbance or contact interaction. A preliminary **S3** session of the two vehicle self-toss maneuver was conducted on-board the ISS in November 2021, as shown in Fig. 16. In addition, presented is the preliminary post-processing position and orientation results from the ISS November 2021 session.

In conclusion, a comparison of the TORO simulation to that of the experimental sessions performed NPS SRL, and Ames IRG session was able to be successfully compared with the **S3** TORO self-toss simulations, and the information gleaned can be used to predict the system response to a range of release angles.

Acknowledgments

Acknowledgment to the Naval Postgraduate School Foundation for their financial support, through which this research has been made possible. This research was performed while the author, Stephen Kwok-Choon, held an NRC Research Associateship at the Spacecraft Robotics Laboratory of the Naval Postgraduate School. Acknowledgment to the Intelligent Robotics Group and team at NASA without which this research would not have been possible.

References

[1] K. P. Alsup. Robotic spacecraft hopping: Application and analysis. M.s. thesis, Dept. of Mech. and Aero. Eng., NPS, Monterey, CA, USA, 2018. [Online].

[2] N. Labeaga-Martínez, M. Sanjurjo-Rivo, J. Díaz-Álvarez, and J. Martínez-Frías. Additive manufacturing for a Moon village. *Procedia Manufacturing*, 13:794–801, jan 2017. DOI: 10.1016/J.PROMFG.2017.09.186.

[3] Miguel E Coto, Cole C Pazar, Benedict Mckeown, and Christopher Shanley. Lunar Regolith Sample Excavation Company - A Space Resources Business Plan. *ASCEND 2021*, nov 2021. DOI: 10.2514/6.2021-4032.

[4] Terry D. Haws, Joshua S. Zimmerman, and Michael E. Fuller. SLS, the Gateway, and a Lunar Outpost in the Early 2030s. *IEEE Aerospace Conference Proceedings*, 2019-March, mar 2019. DOI: 10.1109/AERO.2019.8741598.

[5] Paolo Fiorini and Joel Burdick. The Development of Hopping Capabilities for Small Robots. *Autonomous Robots*, 14(2):239–254, 2003. DOI: 10.1023/A:1022239904879.

[6] Joel Burdick and Paolo Fiorini. Minimalist jumping robots for celestial exploration. *International Journal of Robotics Research*, 22(7-8 SPECIAL ISSUE):653–674, 2003.

[7] T Kubota and T Yoshimitsu. Intelligent rover with hopping mechanism for asteroid exploration. In *2013 6th International Conference on Recent Advances in Space Technologies (RAST)*, pages 979–984, 2013. DOI: 10.1109/RAST.2013.6581357.

[8] Steven Dubowsky, Samuel Kesner, Jean-Sébastien Plante, and Penelope Boston. Hopping mobility concept for search and rescue robots. *Industrial Robot: An International Journal*, 35:238–245, may 2008. DOI: 10.1108/01439910810868561.

[9] Tetsuo Yoshimitsu, Takashi Kubota, and Ichiro Nakatani. MINERVA rover which became a small artificial solar satellite. In *Proceedings of the Small Satellite Conference*, 2006.

[10] Tetsuo Yoshimitsu, Takashi Kubota, Tadashi Adachi, and Yoji Kuroda. Advanced robotic system of hopping rovers for small solar system bodies. In *International Symposium on Artificial Intelligence, Robotics and Automation in Space*, volume 1, pages 3–7, Turin, Italy, 2012.

[11] Ross Allen, Marco Pavone, Christopher McQuin, Issa A.D. Nesnas, Julie C. Castillo-Rogez, Tam Nguyen Nguyen, and Jeffrey A. Hoffman. Internally-actuated rovers for all-access surface mobility: Theory and experimentation. *Proceedings - IEEE International Conference on Robotics and Automation*, pages 5481–5488, 2013. DOI: 10.1109/ICRA.2013.6631363.

[12] Kenji Nagaoka, Riku Takano, Takayuki Izumo, and Kazuya Yoshida. Ciliary Micro-Hopping Locomotion of an Asteroid Exploration Robot. *Proceedings of the 11th International Symposium on Artificial Intelligence, Robotics and Automation in Space*, 2012.

[13] Duncan W Haldane, M M Plecnik, J K Yim, and R S Fearing. Robotic vertical jumping agility via series-elastic power modulation. *Science Robotics*, 1(1), 2016.

[14] J. L. Komma. Mechatronics: The development, analysis, and ground-based demonstrations of robotic spacecraft hopping with a manipulator. M.s. thesis, Dept. of Mech. and Aero. Eng., NPS, Monterey, CA, USA, 2018. [Online].

[15] Stephen Kwok Choon, Jonathan Chitwood, Conor Safbom, Patrick Leary, and Marcello Romano. ASTROBATICS: A Hopping-Manuever Experiment for a Spacecraft-Manipulator System on board the International Space Station. In *70th International Astronautical Congress*, pages 21–25, Washington, DC, 2019. International Astronautical Federation.

[16] C. P. Safbom. Design, testing, and analysis of self-toss hopping maneuvers of astrobee at NPS and NASA ames research center. M.s. thesis, Dept. of Mech. and Aero. Eng., NPS, Monterey, CA, USA, 2020. [Online].

[17] Stephen Kwok-Choon, Conor Safbom, Jonathan Chitwood, Patrick Leary, James Summerlin, Daniel Watanabe, and Jonathan Barlow. Astrobatics : Characterization of Experimental Self-Toss Maneuvers At the Naval Postgraduate School and Nasa Ames: AAS 20-427. In *2020 AAS/AIAA Astrodynamics Specialist Conference(AAS 20-427)*, pages 1–20, 2020.

[18] Stephen Kwok-Choon, Jennifer Hudson, Daniel Watanabe, James Summerlin, Ian Hardy, and Marcello Romano. Astrobatics Session 1: Self-Toss Maneuvers with Astrobee Onboard the International Space Station. In *AAS/AIAA Astrodynamics Specialist Conference, Lake Tahoe, CA, Aug. 9-12 (AAS 21-652)*, page 19, Lake Tahoe, CA, 2021. American Astronautical Society.

[19] Jonathan Chitwood. Design and Analysis of On-orbit Robotic Spacecraft Hopping Maneuvers. M.s. thesis, Naval Postgraduate School, Monterey, CA, USA, 2021.

[20] NASA Ames Intelligent Robotics Group. Astrobee Guest Science Guide. Technical report, National Aeronautics and Space Administration, Moffet Field, CA, 2017.

[21] Simeon Kanis and Brian Dunbar. What is Astrobee? | NASA, 2020. Available at `https://www.nasa.gov/astrobee`.

[22] Trey Smith, Jonathan Barlow, Maria Bualat, Terrence Fong, Christopher Provencher, Hugo Sanchez, and Ernest Smith. Astrobee: A New Platform for Free-Flying Robotics on the ISS. In *Intelligent Robots Group, NASA Ames Research Center*, Moffet Field, CA, 2016. National Aeronautics and Space Administration.

[23] Marcello Romano, David A Friedman, and Tracy J Shay. Laboratory Experimentation of Autonomous Spacecraft Approach and Docking to a Collaborative Target. *Journal of Spacecraft and Rockets*, 44(1):164–173, 2007. DOI: 10.2514/1.22092.

[24] Josep Virgili-Llop, Costantinos Zagaris, H Park, Richard Zappulla II, and Marcello Romano. Experimental Evaluation Of Model Predictive Control And Inverse Dynamics Control for Spacecraft Proximity and Docking Maneuvers. In *6th International Conference on Astrodynamics Tools and Techniques. 14-17 March 2016, Darmstad, Germany.*, 2016.

[25] Richard Zappulla, Josep Virgili-Llop, Costantinos Zagaris, Hyeongjun Park, and Marcello Romano. Dynamic Air-Bearing Hardware-in-the-Loop Testbed to Experimentally Evaluate Autonomous Spacecraft Proximity Maneuvers. *Journal of Spacecraft and Rockets*, 54(4):825–839, apr 2017. DOI: 10.2514/1.A33769.

[26] Josep Virgili-Llop, Costantinos Zagaris, Richard Zappulla, Andrew Bradstreet, and Marcello Romano. Laboratory experiments on the capture of a tumbling object by a spacecraft-manipulator system using a convex-programming-based guidance. *Advances in the Astronautical Sciences*, 162(September):787–807, 2018.

[27] Josep Virgili-Llop and Marcello Romano. Simultaneous Capture and Detumble of a Resident Space Object by a Free-Flying Spacecraft-Manipulator System. *Frontiers in Robotics and AI*, 6(March):14, 2019. DOI: 10.3389/frobt.2019.00014.

[28] R Zappulla, H Park, J Virgili-Llop, and M Romano. Real-Time Autonomous Spacecraft Proximity Maneuvers and Docking Using an Adaptive Artificial Potential Field Approach. *IEEE Transactions on Control Systems Technology*, 27(6):2598–2605, 2019. DOI: 10.1109/TCST.2018.2866963.

[29] R. Zappulla, J. Virgili-Llop, C. Zagaris, H. Park, and M. Romano. Dynamic air-bearing hardware-in-the-loop testbed to experimentally evaluate autonomous spacecraft proximity maneuvers. *Journal of Spacecraft and Rockets*, 54(4):825–839, July 2017.

[30] Stephen Kwok-Choon, Markus Wilde, Conor Safbom, and Marcello Romano. Kinematic and Dynamic Spacecraft Maneuver Simulators for Verification and Validation of Space Robotic Systems. In *AAS/AIAA Astrodynamics Specialist Conference, Lake Tahoe, CA, Aug. 9-12 (AAS 20-424)*, pages 1–20, Lake Tahoe, CA, 2020. AAS/AIAA. DOI: 10.2514/6.2020-1919.

[31] Brian Dunbar and Simeon Kanis. Spheres facilities at NASA AMES. NASA, Aug. 3, 2017. [Online]. Available at https://www.nasa.gov/spheres/spheres-facilities-at-nasa-ames.

[32] Steven Dubowsky and Evangelos Papadopoulos. The Kinematics, Dynamics, and Control of Free-Flying and Free-Floating Space Robotic Systems. *IEEE Transactions on Robotics and Automation*, 9(5):531–543, 1993. DOI: 10.1109/70.258046.

[33] M. Romano. *Orbital Space Robotics: Flight Mechanics of Orbiting Vehicle Manipulator Systems*. Pending, Naval Postgraduate School, first edition, 2022 (planned).

[34] DYNAMIXEL. *XH430-V210-R*, Specifications, 2021. [Online]. Available at https://emanual.robotis.com/docs/en/dxl/x/xh430-v210/.

[35] A. Z. Rao. Realization of dynamixel servo plant parameters to improve admittance control for a compliant human-robot interaction. M.s. thesis, Dept. of Biomedical. Eng., NJIT, Newark, NJ, USA, 2016. [Online].

[36] Ana Guzman. Space Station Science Highlights: Week of November 22, 2021, nov 2021. Available at https://www.nasa.gov/mission_pages/station/research/news/space-station-science-highlights-22nov21.